Cross-scale spatial variability and associations of carbon pools provide insight into regulating carbon sequestration in tropical montane rainforests

Zhangqi Ding[1,2], Zhijian Mou[1,2,3], Yanpeng Li[4], Jun Wang[1,2], Donghai, Wu[1,2], Chao Liang[5], Dafeng Hui[6], Jordi Sardans[7,8,9], Josep Peñuelas[7,8], Han Xu[4*], Zhanfeng Liu[1,2*]

[1]Key Laboratory of Vegetation Restoration and Management of Degraded Ecosystems & CAS Engineering Laboratory for Vegetation Ecosystem Restoration on Islands and Coastal Zones, South China Botanical Garden, Chinese Academy of Sciences, Guangzhou 510650, China

[2]South China National Botanical Garden, Guangzhou 510650, China

[3]College of Resources and Environment, University of Chinese Academy of Sciences, Beijing 100049, China

[4]Research Institute of Tropical Forestry, Chinese Academy of Forestry, Longdong, Guangzhou 510520, China

[5]Key Laboratory of Forest Ecology and Management, Institute of Applied Ecology, Chinese Academy of Sciences, Shenyang 110016, China

[6]Department of Biological Sciences, Tennessee State University, Nashville, TN 37209, USA

[7]CSIC, Global Ecology Unit CREAF-CSIC-UAB, Cerdanyola del Valles, Catalonia 08193, Spain

[8]CREAF, Cerdanyola del Valles, Catalonia 08193, Spain

[9]Nonlinear Analysis and Applied Mathematics (NAAM)-Research Group, Department of Mathematics. Faculty of Science, King Abdulaziz University, P.O. Box 80257, Jeddah 21589, Saudi Arabia

Correspondences:

Zhanfeng Liu, liuzf@scbg.ac.cn; Han Xu, hanxu81@gmail.com;

Cross-scale spatial variability and associations of carbon pools provide insight into regulating carbon sequestration in tropical montane rainforests

Zhangqi Ding[1,2], Zhijian Mou[1,2,3], Yanpeng Li[4], Jun Wang[1,2], Donghai, Wu[1,2], Chao Liang[5], Dafeng Hui[6], Jordi Sardans[7,8,9], Josep Peñuelas[7,8], Han Xu[4*], Zhanfeng Liu[1,2*]

[1]Key Laboratory of Vegetation Restoration and Management of Degraded Ecosystems & CAS Engineering Laboratory for Vegetation Ecosystem Restoration on Islands and Coastal Zones, South China Botanical Garden, Chinese Academy of Sciences, Guangzhou 510650, China

[2]South China National Botanical Garden, Guangzhou 510650, China

[3]College of Resources and Environment, University of Chinese Academy of Sciences, Beijing 100049, China

[4]Research Institute of Tropical Forestry, Chinese Academy of Forestry, Longdong, Guangzhou 510520, China

[5]Key Laboratory of Forest Ecology and Management, Institute of Applied Ecology, Chinese Academy of Sciences, Shenyang 110016, China

[6]Department of Biological Sciences, Tennessee State University, Nashville, TN 37209, USA

[7]CSIC, Global Ecology Unit CREAF-CSIC-UAB, Cerdanyola del Valles, Catalonia 08193, Spain

[8]CREAF, Cerdanyola del Valles, Catalonia 08193, Spain

[9]Nonlinear Analysis and Applied Mathematics (NAAM)-Research Group, Department of Mathematics. Faculty of Science, King Abdulaziz University, P.O. Box 80257, Jeddah 21589, Saudi Arabia

Correspondences:

Zhanfeng Liu, liuzf@scbg.ac.cn; Han Xu, hanxu81@gmail.com;

Abstract

The spatial distribution of plant, soil, and microbial carbon pools, along with their intricate interactions, presents a great challenge for the current carbon cycle research. However, it is not clear what are the characteristics of the spatial variability of these carbon pools, particularly their cross-scale relationships. We investigated the cross-scale spatial variability of microbial necromass carbon (MNC), soil organic carbon (SOC) and plant biomass (PB), as well as their correlation in a tropical montane rainforest using multifractal analysis. The results showed multifractal spatial variations of MNC, SOC, and PB, demonstrating their adherence to power-law scaling. MNC, especially low MNC, exhibited stronger spatial heterogeneity and weaker evenness compared with SOC and PB. The cross-scale correlation between MNC and SOC was stronger than their correlations at the measurement scale. Furthermore, the cross-scale spatial variability of MNC and SOC exhibited stronger and more stable correlations than those with PB. Additionally, our results suggest that when SOC and PB are both low, it is advisable for reforestations to potentiate MNC formation, whereas when both SOC and PB are high some thinning can be advisable to favour MNC formation. Thus, these results support the utilization of management measures such as reforestation or thinning as nature-based solutions to regulate carbon sequestration capacity of tropical forests by affecting the correlations among various carbon pools.

Keywords: Microbial necromass carbon, Spatial variability, Cross-scale, Tropical forests, Multifractal analysis, Joint multifractal analysis

1. Introduction

Forest ecosystems serve as the largest terrestrial organic carbon reservoirs (Eswaran et al., 1993; Alemu, 2014) and play a pivotal role in the global carbon cycle (Mitchard, 2018). Tropical forests store over 60% of global forest carbon in living biomass, necromass, and soil carbon, approximately accounting for 25% of terrestrial biosphere carbon stocks (Bonan, 2008; Pan et al., 2011), and with the highest organic carbon turnover efficiency (Sayer et al., 2019). Microorganisms are critical participants in carbon cycling, establishing a vital connection between plant and soil carbon pools. While soil microorganisms decompose and transform large plant-derived carbon molecules through the secretion of extracellular enzymes (Sinsabaugh et al., 2009), they also assimilate small organic molecules, including easily decomposable organic carbon from plant and microbial sources, and synthesize their biomass through assimilation (Lehmann & Kleber, 2015; Zhu et al., 2018). Subsequently, through cellular processes including growth, reproduction, and death, a portion of the carbon is released into the atmosphere as CO_2 by respiration, while another portion becomes an important component of soil organic carbon (SOC) in the form of necromass carbon (accounting for up to 50%) (Liang et al., 2019; Wang et al., 2021). The accumulation of microbial necromass carbon (MNC) represents a balance between microbial decomposition and assimilation processes and serves as a key factor affecting the dynamic changes of soil carbon stocks. Investigating the spatial variability of different carbon pools in tropical forests, especially the association between MNC and SOC and plant biomass (PB), using soil microorganisms as a link, is an effective approach for understanding and managing forest carbon stocks and cycling.

Compared with the studies on SOC and PB at a global scale, current research on the spatial variation of MNC has mainly concentrated on temperate and subtropical regions (Mou et al., 2021; Wang et al., 2021; Yang et al., 2020). These studies are usually based

on fixed measurement scales to reveal the spatial distribution and control of SOC, PB or MNC, while the association between the three across spatial scales remains uncertain (Li W. et al., 2023; Li Y. et al., 2023). Moreover, previous studies on spatial patterns of variables have mostly been based on the concept of moving windows, such as wavelet analysis (Keitt, 2008), trend-surface analysis (Zhang et al., 2022), and semi-variogram analysis (Haruna, 2021) based on fractal dimension. These methods are primarily used to determine the multi-scale characteristics and corresponding intensities of variable spatial distributions, but they cannot identify the cross-scale patterns in the spatial distributions of variables, i.e., scaling properties. This hinders the numerical simulations of various carbon pool spatial distribution models, particularly in capturing changes in the associations between pairs of variables during the downscaling or upscaling processes in multi-variable models.

Fractal analysis and multifractal analysis are more effective for describing the spatial variability and scaling features of variables (Caniego et al., 2005). By revealing the multi-scale self-similarity of variables, they can provide insights into the intrinsic correlation between wholes and parts in patterns or features (Cheng, 1999; Zhang et al., 2006). Furthermore, based on variable spectrum visualization, joint multifractal analysis can be further employed to describe the multi-scale joint distribution characteristics of multiple variables in the same spatial domain. Joint multifractal analysis has been used to characterize the correlation between grassland productivity and topographic index (Banerjee et al., 2011), the influence of temperature and nitrogen dioxide on tropospheric ozone (Pavón-Domínguez et al., 2015), and the effects of topography and soil texture on soil water storage (Biswas, 2019). However, whether changes in spatial scales would alter the spatial variability of MNC by influencing the relative strength or dominance of various ecological processes (such as the scaling features of plant and microbial biomass and SOC)

remain unclear, particularly in tropical forests, which are key regions for global carbon cycling.

We hypothesize that MNC, being a significant contributor to SOC, will consistently exhibit a strong positive correlation with SOC. PB, as a primary food resource for microorganisms, may potentially demonstrate parallel spatial variation with MNC at specific scales by influencing the microbial community. To test this, we investigated the spatial distribution of microbial necromass carbon (MNC), soil organic carbon (SOC), and aboveground plant biomass (PB) in a 60-ha plot in tropical montane rainforest. Multifractal analysis and joint multifractal analysis provided a more detailed and comprehensive depiction of the correlations between MNC, SOC, and PB by amplifying and differentiating the high and low values of variables, and integration analysis across multiple spatial scales. This work contributes to our understanding of forest carbon cycling mechanisms and the construction of prediction models.

2. Material and methods

2.1 Study site

This study was conducted at a 60-ha forest dynamic monitoring site located in the tropical montane rainforest of Jianfengling Nature Reserve (JFL), Hainan Province, China (Figure 1). The geographical coordinates of the study area are 108.9050°E, 18.7309°N, with an elevation varies approximately from 866 m to 1017 m. This region falls within the tropical island monsoon climate zone, characterized by two distinct seasons: the rainy season from May to October, and the dry season from November to April. The mean annual precipitation is 2449 mm, and the mean annual temperature is 19.8°C. The lowest and highest monthly average temperatures are 10.8°C and 27.5°C, respectively. The study area is subject to minimal anthropogenic disturbance and remains in its original forested state. For further detailed information on this site, please refer to the ForestGEO

(https://forestgeo.si.edu/sites/asia/hainan).

2.2 Sample collection and indicator determination

We divided the JFL 60-ha (1000 m × 600 m) study site into 500 quadrats (40 m × 30 m) and collected soil samples from each quadrat (Figure 1). Twelve soil cores of the topsoil (0-10 cm) were sampled using a soil auger from a 10 m × 10 m grid within each quadrat, and mixed to form one composite sample per quadrat, resulting in a total of 500 representative soil samples. All soil samples were obtained in 2013. After removing roots, gravel, and other debris using a sieve of 2 mm mesh, soil samples were air-dried at room temperature for further analysis of amino sugars and physicochemical indicators. Soil moisture content was determined by weighing soil after drying in an oven at 105°C for 48 hours. Soil organic carbon (SOC) was determined using potassium dichromate oxidation (Walkley & Black, 1934).

Microbial necromass carbon (MNC) was determined based on the three amino sugar biomarkers (glucosamine, GluN; galactosamine, GalN; and muramic acid, MurN), following the theoretical background and formula proposed by Liang et al. (2019), and extracted and quantified according to the method of Indorf et al. (2011). GluN, GalN, and MurN were identified and quantified using a Dionex RS 3400 fluorescence detector (high-performance liquid chromatography, Dionex Ultimate 3000, Thermo Fisher Scientific, Waltham, USA). In this study, fungi-derived and bacteria-derived microbial necromass carbon were calculated separately and then summed to obtain the total MNC.

Plant biomass was measured based on 20 m × 20 m quadrat survey data, and then transformed to 40 m × 30 m quadrat based on their coordinates. Here, we use the sum of the basal area of all trees within the quadrat to characterize plant biomass.

To facilitate subsequent multifractal analysis and joint multifractal analysis calculations, we discarded one column of quadrats on the right side of the plot and selected

480 contiguous quadrats (24 in the east-west direction and 20 in the north-south direction) for analysis.

2.3 Correlation analysis

We examined the direct correlation between MNC, SOC, and PB. For the calculation, we used the "Kolmogorov-Smirnov" test to determine whether each variable followed a normal distribution. The Pearson correlation coefficient was used when the data followed a normal distribution, while the Spearman correlation coefficient was selected otherwise.

2.4 Multifractal and Joint multifractal analysis

Multifractal analysis has been used to characterize the spatial or temporal variability of data sets either on one-dimensional or two-dimensional supports (Stanley & Meakin, 1988), while joint multifractal analysis is commonly used to explore the association features of the scaling characteristics among multiple variables in the same geometric frame (Meneveau et al., 1990). In this study, based on the geometric support of 480 quadrats and referring to the box-counting idea, the entire plot was progressively divided into non-overlapping regions of size δ, consisting of N (such as 1, 2, ..., 480) regions. Here, the minimum segmented area δ_{min} is 1200 m^2 (40 m × 30 m), and the maximum segmented area δ_{max} is 576,000 m^2 (480 × 40 m × 30 m). Using the moment method (Halsey et al., 1986), we obtained the partition function $\chi(q, \delta)$, which is determined by the statistical moments order q.

Then, the generalized fractal dimension or Rényi dimension, D_q, can be directly calculated through the order q and the mass exponent function $\tau(q)$ (Hentschel & Procaccia, 1983). $\tau(q)$ was calculated from the slopes of a log–log plot of the partition function and the spatial scale δ at different q values. Several parameters have been extensively employed to describe multifractality features, including D_0 (capacity dimension), D_1 (entropy dimension), and D_2 (correlation dimension), which are derived from D_q. Considering that

the data of the three carbon pools are distributed across all quadrats, the result for D_0 will be the constant 1. D_1 represents the degree of disorder of variable distribution, e.g., a larger value reflects a more evenness distributed SOC. D_2, reflects the uniformity of measured variable values among local areas. Larger values indicate smaller differences in variable measurements between various local areas, i.e., more homogeneous of SOC. The multifractal spectrum, $f(\alpha)$, is defined as the Hausdorff fractal dimension of the variable that possesses a certain Lipschitz-Hölder or coarse singularity exponent, α, within a sub-plot at scale δ. The correlation between the multifractal function $f(\alpha)$ and α can be computed through Legendre transformation (Evertsz & Mandelbrot, 1992).

In this study, we used the three-variate joint multifractal analysis, which combines the strange attractor formalism and the method of moments (Halsey et al., 1986; Meneveau et al., 1990; Pavón-Domínguez et al., 2015). Similar to multifractal analysis, the entire plot is progressively divided into non-overlapping regions of size δ, consisting of N (such as 1, 2, ..., 480) regions. Similar to multifractal analysis, we also selected the Legendre transformation to calculate the singularity exponent α of SOC, PB, and MNC for different combinations of order $q_{[SOC]}$, $q_{[PB]}$, and $q_{[MNC]}$. The $f(\alpha_{[SOC]}, \alpha_{[PB]}, \alpha_{[MNC]})$ can be viewed as the fractal dimension of the set of intervals based on the combinations of $\alpha_{[SOC]}$, $\alpha_{[PB]}$, and $\alpha_{[MNC]}$ with different $q_{[SOC]}$, $q_{[PB]}$, and $q_{[MNC]}$.

For detailed definitions and calculations of indicators in multifractal analysis and joint multifractal analysis, please refer to the Appendix. The joint multifractal analysis was conducted in R (R, 2021) (version 4.1.2) after modifying the pseudo-code programming language provided by Pavón-Domínguez et al. (2015).

3. Results

3.1 Statistical analysis of MNC, SOC, and PB

In this study, the K-S test showed that MNC and PB followed a normal distribution, but

SOC did not. Therefore, Spearman correlation coefficients were used in the bivariate correlation analysis of MNC, SOC, and PB. The linear correlations between MNC, SOC, and PB are shown in Figure 2. As one of the vital components of SOC, MNC exhibited a strong positive correlation with SOC (r = 0.7, p < 0.001). In contrast, although the correlation between MNC and PB was statistically significant (p < 0.01), it was very weak (r = 0.13), which might be attributed to the larger sample size utilized in this study. The spatial distributions of MNC, SOC and PB are shown in Figure S1.

3.2 Multifractal analysis of MNC, SOC, and PB

We examined the multifractal characteristics under different conditions of order q by investigating the correlation between the partition function $\chi(q, \delta)$ and spatial resolution δ. We evaluated the spatial heterogeneity of MNC, SOC, and PB using generalized dimension spectra (D_q - q) and singular spectra ($f(\alpha)$ - α) (Figure 3). The log–log scatter plots of the partition functions for MNC, SOC, and PB with spatial resolution showed that the linear fitting coefficients of determination R^2 from $\delta_{[min]}$ = 1 × 1,200 m^2 to $\delta_{[max]}$ = 480 × 1,200 m^2 were all greater than 0.999 (Figure S2), indicating multifractal characteristics in the spatial variation of these three variables. The D_q curves exhibited a sigma shape for all three variables. Some parameters (e.g., D_0, D_1, D_2, α_{min}, and α_{max}) of interest are listed in Table 1. The D_q curves for MNC, SOC, and PB all crossed 1.00 at q = 0, and reached their maximum and minimum values at q = −30 and q = 30, respectively. The entropy dimension D_1 ranged from 0.993 to 0.996, and the correlation dimension D_2 ranged from 0.987 to 0.995 (Table 1). The Rényi dimensions of MNC, SOC, and PB exhibited good scaling trends. The range of variation in the generalized dimension spectra, ΔD (D_{-30}–D_{30}), showed that MNC had a larger curvature magnitude, with the smallest magnitude observed for PB. This indicates that the spatial heterogeneity of MNC was greater than that of SOC and PB. Although MNC, SOC, and PB exhibited strong power-law scaling, their multifractality still

differed. Compared with high PB, the multifractal features of high MNC and high SOC were more similar. The similarities and differences between the capacity dimension D_0, entropy dimension D_1, and correlation dimension D_2 are commonly used to assess the scaling features of variables. In this study, across all three D_q curves, $D_0 > D_1 > D_2$ (Table 1). Compared with SOC and PB, the spatial distribution of MNC tended to be more multifractal.

The singular spectra of MNC, SOC, and PB exhibited a "bell-shaped" distribution, and the width and height of the curves reflected the similarity or difference in local-scale patterns of these three variables. After scaling the positive and negative values of order q, the left and right branches (L and R) of the singular spectrum were linked with larger and smaller values of the observed variables, respectively. Differences existed in the upward amplitude of the left branch and the downward amplitude of the right branch between SOC and MNC, and they were not completely symmetrical. The slight left skewness of SOC implies that larger values dominated, or extreme maximum values existed in its spatial variability, while the slight right skewness in MNC indicates that smaller values dominated or had extreme minimum values. The long lower left branch of SOC indicates that the regions covering high SOC content were small and rare, suggesting strong spatial heterogeneity. In other words, the high values in SOC tended to cluster, while the spatial distribution of low values was more dispersed and even. Similar to the variation amplitude of D_q, the wider the singularity spectrum, represented by the width $\Delta\alpha$ ($\alpha_{max}-\alpha_{min}$), the more apparent the multifractality of the spatial distribution and the larger the spatial variability of the variable. Therefore, spatial distributions of MNC and PB exhibited the highest and lowest scaling heterogeneity, respectively. The maximum value of the singular spectra, $f(\alpha_0)$, corresponds to the capacity dimension D_0 of the generalized dimension spectrum.

3.3 Joint multifractal analysis of MNC, SOC, and PB

We investigated the correlation between spatial resolution and the joint partition function of MNC, SOC, and PB based on scenarios involving different combinations of the order q. The linear correlation indicated that the spatial distribution of MNC, SOC, and PB was multifractal. Considering that the generalized dimension spectrum of MNC, SOC, and PB all reached a steady state at $q = \pm 30$, and their relative variations stabilized when $q = 15$ (Figure 3). Therefore, to expedite the entire computation process while ensuring an accurate description of the correlation between the variables, we selected the interval of q values as [−15, 15]. The joint multifractal spectrum (Figure 4a) showed the fractal dimension $f(\alpha_{[MNC]}, \alpha_{[SOC]}, \alpha_{[PB]})$, corresponding to the intervals of each singularity exponential combination of $\alpha_{[MNC]}$, $\alpha_{[SOC]}$, and $\alpha_{[PB]}$. The joint multifractal spectrum was a set of surfaces formed based on different q values (e.g., Figure 4b and c). Once a specific q value for a variable was chosen, the corresponding slice could be obtained from the joint multifractal spectrum. The variation characteristics of slices could be analysed based on the correlations established between the other two variables (Figure 5). Furthermore, when all three exponents were zero ($q_{[MNC]} = 0$, $q_{[SOC]} = 0$, $q_{[PB]} = 0$), $f(\alpha_{[MNC]}, \alpha_{[SOC]}, \alpha_{[PB]})$ in the joint multifractal spectrum, which corresponded to the capacity dimension supported by the spatial extent would reach the maximum value of 1. Similar to the singularity spectra in multifractal analysis, the wider the range between α_{max} and α_{min}, the stronger multifractal properties exhibited by the spatial distribution of variables, indicating higher spatial variability.

Here, we selected scenarios with $q_{[PB]}$ of −15, 0, and 15, respectively. The first row of Figure 5 shows the projection of slices of the joint multifractal spectrum onto the $\alpha_{[MNC]}$-$\alpha_{[SOC]}$ plane for the corresponding $q_{[PB]}$ value. When high values of $q_{[PB]}$ or $q_{[SOC]}$ were chosen, the focus of the analysis was on the response of partial data of the variable under these conditions, rather than the all values of the variables. For instance, $q_{[PB]} = 15$ indicates a scenario with high above-ground plant biomass, while $q_{[PB]} = -15$ represents a low plant

biomass scenario, and $q_{[PB]} = 0$ corresponds to the bivariate joint multifractal analysis investigation of MNC and SOC. The results show that when $q_{[PB]} = 15$ and −15, the maximum values of $f(\alpha_{[MNC]}, \alpha_{[SOC]}, \alpha_{[PB]})$ in the joint multifractal spectrum of MNC and SOC were 0.61 and 0.66, respectively, lower than the theoretical maximum of 1. On the whole, $\alpha_{[MNC]}$ and $\alpha_{[SOC]}$ exhibited a strong positive correlation ($r = 0.90$, $p < 0.001$), which was greater than the coefficient of correlation between MNC and SOC at the measurement scale. When $q_{[SOC]} \geqslant 0$, the spectra showed a clear direction from the lower left to the top right; when $q_{[SOC]} < 0$, this trend was only observed in the scenario with $q_{[PB]} = 15$. These findings demonstrate a strong association between high SOC and MNC, regardless of the level of PB. However, a strong correlation between low SOC and MNC was only observed when PB was very high. In the bottom left of the spectrum, low $\alpha_{[MNC]}$ and $\alpha_{[SOC]}$ values suggest that high MNC was associated with high SOC. In the top right of the spectrum, a correlation between low MNC and low SOC was established as indicated by high $\alpha_{[MNC]}$ and $\alpha_{[SOC]}$ values. Thus, the well-known strong correlation between MNC and SOC remained consistent across all spatial scales, albeit slightly weaker when SOC was very low. Additionally, $f(\alpha_{[MNC]}, \alpha_{[SOC]}, \alpha_{[PB]})$ values varied from large to small in the bottom left and top right regions of the multifractal spectrum, signifying a large heterogeneity in the spatial interval of combinations with high SOC and high MNC, as well as low SOC and low MNC.

We also investigated the scaling relationship between PB and MNC by selecting scenarios with $q_{[SOC]}$ of −15, 0, and 15. The slice of the joint multifractal spectrum corresponding to the value of $q_{[PB]}$ (Figure 4c) intersected with the slice of $q_{[SOC]}$ (Figure 4b), forming the edge and centre dots in Figure 5 (represented by green, yellow, and blue dots). Overall, unlike SOC, the correlation between MNC and PB was very weak ($r = 0.09$, $p < 0.01$). When SOC was low (e.g., $q_{[SOC]} = -15$), MNC was positively correlated with

high PB (e.g., $q_{[PB]} = 15$), but negatively correlated with low PB ($q_{[PB]} = -15$). Conversely, when SOC was high ($q_{[SOC]} = 15$), the correlation between MNC and PB changed; MNC became negatively correlated with high PB, but positively correlated with low PB. Therefore, as demonstrated when $q_{[SOC]} = 0$, the correlation between MNC and PB was not constant but depended on the levels of PB and MNC. In general, when PB and MNC were both high or both low, they were negatively correlated, which may be related to the high or low SOC content in those areas. On the other hand, when one of the variables, either PB or MNC, was at a lower level, they were positively correlated, which may also be influenced by the local SOC. Furthermore, the difference between high and low SOC in the joint multifractal spectra was reflected in the spectra extending towards the left and right regions ($\alpha_{[MNC]}$ is 0.89 and 1.15, respectively). This suggests that regardless of the level of PB, high SOC leads to high MNC, whereas the presence of low SOC would be accompanied by lower MNC, further highlighting the strong correlation between SOC and MNC.

When neither SOC nor PB was considered, i.e., when both $q_{[SOC]}$ and $q_{[PB]}$ were zero, the projection of joint multifractal spectra of MNC, was represented by circular dots in Figure 6, as well as the yellow dots in the middle column of Figure 5. Theoretically, the numerical variations should be identical to the results of the singularity spectra for MNC mentioned in the previous section (with slight differences in this paper due to different ranges of $q_{[MNC]}$). Figure 6 shows that for different combinations of q values (−15, 0, 15) for SOC and PB, the $f(\alpha_{[MNC]}, \alpha_{[SOC]}, \alpha_{[PB]})$ values of MNC's single multifractal spectra were all lower than 1. Compared with the combination of $q_{[SOC]} = -15$ and $q_{[PB]} = 15$, the $f(\alpha_{[MNC]}, \alpha_{[SOC]}, \alpha_{[PB]})$ values for other combinations of $q_{[SOC]}$ and $q_{[PB]}$ were relatively lower. This suggests that, compared with scenarios with low SOC and high PB, the range of MNC covered in other combination scenarios was relatively small, indicating a greater spatial heterogeneity and a stronger influence on MNC. When $q_{[SOC]} = -15$, the right branch of

MNC's single multifractal spectra was significantly longer than the left branch and higher $\alpha_{[MNC]}$ indicated very low MNC under this condition, despite the lower $f(\alpha_{[MNC]}, \alpha_{[SOC]}, \alpha_{[PB]})$ values indicating a lower occurrence frequency. However, when $q_{[SOC]} = 15$, the left branch of MNC's single multifractal spectra was noticeably longer than the right branch, and smaller $\alpha_{[MNC]}$ indicated a very high MNC under this condition, although its probability of occurrence was also low. Furthermore, when the SOC was low ($q_{[SOC]} = -15$), the variability of MNC was also reduced. In the case of low SOC and low PB, the content of MNC was more even, which could also be observed from the narrower spectrum.

When only one variable such as SOC (or PB) was considered, that is, $q_{[PB]} = 0$ (or $q_{[SOC]} = 0$), the three-variate joint multifractal analysis turned into a bivariate joint multifractal analysis. The projection of MNC's joint multifractal spectrum is shown in Figure 6b, and the yellow dots in the left and right columns of Figure 5. In comparison with $q_{[SOC]} = -15$ and $q_{[PB]} = 0$, the $f(\alpha_{[MNC]}, \alpha_{[SOC]}, \alpha_{[PB]})$ values for other combinations of $q_{[SOC]}$ and $q_{[PB]}$ were relatively low. This suggests that compared with low SOC, the interval covering MNC in other scenarios was quite small, indicating a greater spatial heterogeneity and a stronger influence on MNC. When $q_{[SOC]} = -15$ and $q_{[PB]} = 0$, or $q_{[SOC]} = 0$ and $q_{[PB]} = \pm 15$, the right branch of MNC's single multifractal spectra was significantly longer than the left branch, and higher $\alpha_{[MNC]}$ indicated extremely low MNC under these conditions, with a lower probability of occurrence. However, when $q_{[SOC]} = 15$ and $q_{[PB]} = 0$, the left branch of MNC's single multifractal spectra was significantly longer than the right branch, and smaller $\alpha_{[MNC]}$ indicated extremely high MNC under this condition, despite its minimal probability of occurrence. Compared with PB, the SOC content significantly amplified the difference between the left and right branches of MNC's single multifractal spectra, exerting a stronger effect on MNC extremes.

4. Discussion

In forest ecosystems, carbon cycling was affected by multiple factors, and the spatial distribution and variability characteristics (such as multifractal structures) of different forms of carbon storages (e.g., MNC, SOC, and PB) were the result of the nested effects of various biotic and abiotic factors and ecological processes (Puglielli et at., 2021). The variability of MNC, SOC, and PB was lower than that of various soil physicochemical factors measured at the fine scale by Siqueira et al. (2018). This might be attributed to the higher complexity of environmental and ecological processes at smaller scales, resulting in increased heterogeneity of carbon distribution. Exploring their spatial variability at different scales using the multifractal analysis could improve the spatial interpolation models for predicting different forms of carbon, which is crucial for understanding forest carbon cycling pathways or carbon stock assessments. In general, if the spatial distribution of a variable is primarily responsive to a linear process, a single coefficient can be performed to interpolate at multiple scales, meaning that standard methods can be employed (Siqueira et al., 2018). However, if the spatial pattern is influenced by multi-scales and nonlinear regulation of multiple factors and processes, it is necessary to use the multifractal analysis to estimate multiple scaling indices to quantify its variability and use higher-order singularity exponents for model prediction and estimation (e.g., $|q| > 2$). Overall, the distribution structure and multifractal characteristics of different carbon storage forms (MNC, SOC, and PB) were not entirely identical within the same spatial extent in the studied tropical forest ecosystems. The multifractal analysis effectively described the spatial variation of different carbon storage forms in tropical rainforests, revealing and distinguishing their similarities and differences, thus being a more exact descriptor of the real relationships.

Numerous studies have indicated that MNC is an important component of SOC. Although its proportion in forests is lower than that in crop and grassland ecosystems, it

can still reach up to 50% (Liang et al., 2019; Wang et al., 2021). The multifractal features of high MNC and high SOC in tropical rainforests were highly similar, and the strong positive correlation between them in the joint multifractal analysis also confirmed this cross-scale dependency. Fertile soil can promote the growth and reproduction of microbial communities, which is more conducive to the accumulation of MNC (Zhou et al., 2023). However, the correlation between SOC and MNC weakened with decreasing SOC, particularly when PB was very low. This may be due to the higher variable proportion of MNC in SOC, and the higher activity of MNC compared with that of mineral-associated organic carbon (MAOC) (Kou et al., 2023), which makes it more readily available for microbial reutilization. Nutrient-poor habitats formed by low PB and SOC may drive microorganisms toward the decomposition of existing necromass carbon to meet their own growth and reproduction needs (Buckeridge et al., 2022; Zhang et al., 2021). Moreover, under low PB, the contribution of plant exudates can also be very variable depending on the few species present of depending on whether the low biomass is due to the lower density of large/adult trees or a lot of small/young trees. Thus, disrupted balance in MNC accumulation leads to a decrease in the parallel variations of MNC and SOC.

In general, vegetation increases the carbon input in the soil through litter or root exudates, which changes microbial growth, reproduction, and diversity, thereby affecting the accumulation of MNC (Prommer et al., 2019). However, due to probably the priming effect and differences in the utilization efficiency of different carbon sources, MNC often fails to change in synergy with aboveground vegetation biomass, forming a significant positive correlation (Ma et al., 2018; Mou et al., 2021). The multifractal structure of MNC and PB exhibit lower similarity than that of SOC. Moreover, the cross-scale correlation between MNC and PB is slightly weaker than that at the measurement scale, which is exactly the opposite of the stronger correlation between MNC and SOC at the cross-scale.

When PB is high, although the total SOC is also high, it may be dominated by plant-derived organic carbon such as lignin, which is slow to decompose. Coupled with the presence of strong positive priming effects, MNC decreases due to its susceptibility to rapid decomposition (Cui et al., 2020). When both PB and SOC were at low levels, larger areas of forest gaps in the quadrats may be conducive to the utilization of fast-growing and dominant shrub or herbaceous plants by microorganisms, thus promoting the accumulation of MNC (Wang et al., 2021). Both scenarios lead to a clear negative correlation between PB and MNC. Overall, this non-stationary relationship between MNC and PB is closely correlated with the differential availability of various types of carbon in the soil.

Microbial necromass is an important source of soil organic matter (SOM), and conventional analysis at measurement scales indicates that MNC is related to aboveground vegetation diversity and biomass, as well as soil physicochemical properties (Mou et al., 2021; Prommer et al., 2019). Joint multifractal analysis provides a more detailed and comprehensive depiction of the correlations between MNC, SOC, and PB in tropical montane rainforests by amplifying and differentiating the high and low values of variables based on the adjustment of order q, and integration analysis across multiple spatial scales. Based on their correlation, we surmise that reforestation in areas with low soil fertility and low tree density in tropical forest ecosystems will likely increase MNC content. However, appropriate thinning may promote MNC accumulation in situations where basal area density and SOC are particularly high. Furthermore, we suggest that SOC can serve as a good indicator of MNC variability when considering carbon cycling processes involving microbial carbon, but we should be cautious where SOC is at extremely low levels. Overall, investigating and understanding the cross-scale associations of MNC, SOC, and PB using joint multifractal analysis contributes to a better comprehension of forest carbon cycling patterns, with positive implications for agricultural cultivation, forestry management, and

mitigation of global warming and climate change.

In summary, we made a significant advancement by substantiating the presence of the multifractal distribution in the spatial distribution of three forms of the carbon pool (MNC, SOC, and PB) in tropical rainforests, and by exploring their cross-scale associations. Notably, MNC displayed stronger heterogeneity, yet weaker evenness compared with SOC and PB. The spatial variability of MNC was strongly reflected in that of SOC, while the cross-scale correlation between PB and MNC was weak. Our results based on multifractal analysis and joint multifractal analysis offered a more comprehensive reflection of the variability patterns of carbon in tropical forests, highlighting the necessity to employ higher orders when dealing with spatial interpolation of different carbon pools. Furthermore, SOC could be incorporated as a predictor of MNC into carbon-related models involving microbial involvement. In light of these outcomes, we propose plausible forestry management strategies that are condition-dependent, which may enhance the soil carbon sink capacity in tropical forests. Specifically, our results suggest that when SOC and PB are both low, reforestations is advised to enhance MNC formation, whereas when both SOC and PB are high some thinning is advisable to favour MNC formation. Further validation work needs to be conducted at various spatial scales and ecosystems to deepen insights into the global distribution patterns and cycling mechanisms of carbon.

Acknowledgments

We thank Hans Lambers for language improvement. This work was supported by the Guangdong Flagship Project of Basic and Applied Basic Research (2023B0303050001), the National Natural Science Foundation of China (42177289 and U22A20449), the Spanish Government Grants PID2019-110521GB-I00, PID2020115770RB-I and TED2021-132627B-I00 funded by MCIN, AEI/10.13039/501100011033 European Union

NextGenerationEU/PRTR, the Catalan Government Grant SGR2021-1333, and the Fundación Ramón Areces Grant CIVP20A6621.

Data availability

The data that support the findings of this study are available from the corresponding author upon reasonable request.

References

[1] Alemu, B., 2014. The role of forest and soil carbon sequestrations on climate change mitigation. Research Journal of Agriculture and Environmental Management, 3, 492-505.

[2] Banerjee, S., He, Y., Guo, X., & Si, B. C., 2011. Spatial relationships between leaf area index and topographic factors in a semiarid grassland: Joint multifractal analysis. Australian Journal of Crop Science, 5, 756-763. https://search.informit.org/doi/10.3316/informit.282303442956874

[3] Biswas, A., 2019. Joint multifractal analysis for three variables: Characterizing the effect of topography and soil texture on soil water storage. Geoderma, 334, 15-23. https://doi.org/10.1016/j.geoderma.2018.07.035

[4] Bonan, G. B., 2008. Forests and climate change: forcings, feedbacks, and the climate benefits of forests. Science, 320, 1444-1449. https://doi.org/10.1126/science.1155121

[5] Buckeridge, K. M., Creamer, C., & Whitaker, J., 2022. Deconstructing the microbial necromass continuum to inform soil carbon sequestration. Functional Ecology, 36, 1396-1410. https://doi.org/10.1111/1365-2435.14014

[6] Caniego, F. J., Espejo, R., Martın, M. A., & San José, F., 2005. Multifractal scaling of soil spatial variability. Ecological Modelling, 182, 291-303.

https://doi.org/10.1016/j.ecolmodel.2004.04.014

[7] Cheng, Q., 1999. Multifractality and spatial statistics. Computers & Geosciences, 25, 949-961.

[8] Cui, J., Zhu, Z., Xu, X., Liu, S., Jones, D. L., Kuzyakov, Y., ... & Ge, T., 2020. Carbon and nitrogen recycling from microbial necromass to cope with C: N stoichiometric imbalance by priming. Soil Biology and Biochemistry, 142, 107720. https://doi.org/10.1016/j.soilbio.2020.107720

[9] Eswaran, H., Van Den Berg, E., & Reich, P., 1993. Organic carbon in soils of the world. Soil Science Society of America Journal, 57, 192-194. https://doi.org/10.2136/sssaj1993.03615995005700010034x

[10] Evertsz, C. J., & Mandelbrot, B. B., 1992. Self-similarity of harmonic measure on DLA. Physica A: Statistical Mechanics and its Applications, 185, 77-86. https://doi.org/10.1016/0378-4371(92)90440-2

[11] Halsey, T. C., Jensen, M. H., Kadanoff, L. P., Procaccia, I., & Shraiman, B. I., 1986. Fractal measures and their singularities: The characterization of strange sets. Physical Review A, 33, 1141. https://doi.org/10.1103/PhysRevA.33.1141

[12] Haruna, S. I., 2021. Spatial and fractal characterization of selected soil nutrients along a catena. Catena, 204, 105443. https://doi.org/10.1016/j.catena.2021.105443

[13] Hentschel, H. G. E., & Procaccia, I., 1983. The infinite number of generalized dimensions of fractals and strange attractors. Physica D: Nonlinear Phenomena, 8, 435-444. https://doi.org/10.1016/0167-2789(83)90235-X

[14] Indorf, C., Dyckmans, J., Khan, K. S., & Joergensen, R. G., 2011. Optimisation of amino sugar quantification by HPLC in soil and plant hydrolysates. Biology and Fertility of Soils, 47, 387-396. https://doi.org/10.1007/s00374-011-0545-5

[15] Keitt, T. H., 2008. Coherent ecological dynamics induced by large-scale disturbance.

Nature, 454, 331-334. https://doi.org/10.1038/nature06935

[16] Kou, X., Morriën, E., Tian, Y., Zhang, X., Lu, C., Xie, H., ... & Liang, C., 2023. Exogenous carbon turnover within the soil food web strengthens soil carbon sequestration through microbial necromass accumulation. Global Change Biology, 29, 4069– 4080. https://doi.org/10.1111/gcb.16749

[17] Li, W., Liu, Y., Guo, Z., Li, Y., Hou, Y., Long, Y., ... & Li, Z., 2023. Divergent control and variation in bacterial and fungal necromass carbon respond to the abandonment of rice terraces. Journal of Environmental Management, 344, 118617. https://doi.org/10.1016/j.jenvman.2023.118617

[18] Li, Y., Wang, B., Zhang, Y., Ao, D., Feng, C., Wang, P., ... & An, S., 2024. Afforestation increased the microbial necromass carbon accumulation in deep soil on the Loess Plateau. Journal of Environmental Management, 349, 119508. https://doi.org/10.1016/j.jenvman.2023.119508

[19] Liang, C., Amelung, W., Lehmann, J., & Kästner, M., 2019. Quantitative assessment of microbial necromass contribution to soil organic matter. Global Change Biology, 25, 3578-3590. https://doi.org/10.1111/gcb.14781

[20] Ma, T., Zhu, S., Wang, Z., Chen, D., Dai, G., Feng, B., ... & Feng, X., 2018. Divergent accumulation of microbial necromass and plant lignin components in grassland soils. Nature Communications, 9, 3480. https://doi.org/10.1038/s41467-018-05891-1

[21] Meneveau, C., Sreenivasan, K. R., Kailasnath, P., & Fan, M. S., 1990. Joint multifractal measures: Theory and applications to turbulence. Physical Review A, 41, 894. https://doi.org/10.1103/PhysRevA.41.894

[22] Mitchard, E. T., 2018. The tropical forest carbon cycle and climate change. Nature, 559, 527-534. https://doi.org/10.1038/s41586-018-0300-2

[23] Mou, Z., Kuang, L., He, L., Zhang, J., Zhang, X., Hui, D., ... & Liu, Z., 2021. Climatic

and edaphic controls over the elevational pattern of microbial necromass in subtropical forests. Catena, 207, 105707. https://doi.org/10.1016/j.catena.2021.105707

[24] Pan, Y., Birdsey, R. A., Fang, J., Houghton, R., Kauppi, P. E., Kurz, W. A., ... & Hayes, D., 2011. A large and persistent carbon sink in the world's forests. Science, 333, 988-993. https://doi.org/10.1126/science.1201609

[25] Pavón-Domínguez, P., Jiménez-Hornero, F. J., & Gutiérrez de Ravé, E., 2015. Joint multifractal analysis of the influence of temperature and nitrogen dioxide on tropospheric ozone. Stochastic Environmental Research and Risk Assessment, 29, 1881-1889. https://doi.org/10.1007/s00477-014-0973-5

[26] Prommer, J., Walker, T. W., Wanek, W., Braun, J., Zezula, D., Hu, Y., ... & Richter, A., 2020. Increased microbial growth, biomass, and turnover drive soil organic carbon accumulation at higher plant diversity. Global Change Biology, 26, 669-681. https://doi.org/10.1111/gcb.14777

[27] Puglielli, G., Laanisto, L., Poorter, H., & Niinemets, Ü., 2021. Global patterns of biomass allocation in woody species with different tolerances of shade and drought: evidence for multiple strategies. New Phytologist, 229, 308-322. https://doi.org/10.1111/nph.16879

[28] R Core Team., 2021. Version 4.1.2. R: A Language and Environment for Statistical Computing. R Foundation for Statistical Computing, Vienna, Austria. https://www.R-project.org/

[29] Sayer, E. J., Lopez-Sangil, L., Crawford, J. A., Bréchet, L. M., Birkett, A. J., Baxendale, C., ... & Schmidt, M. W., 2019. Tropical forest soil carbon stocks do not increase despite 15 years of doubled litter inputs. Scientific Reports, 9, 18030. https://doi.org/10.1038/s41598-019-54487-2

[30] Sinsabaugh, R. L., Hill, B. H., & Follstad Shah, J. J., 2009. Ecoenzymatic stoichiometry of microbial organic nutrient acquisition in soil and sediment. Nature, 462, 795-798. https://doi.org/10.1038/nature08632

[31] Siqueira, G. M., Silva, Ê. F., Vidal-Vázquez, E., & Paz-González, A., 2018. Multifractal and joint multifractal analysis of general soil properties and altitude along a transect. Biosystems Engineering, 168, 105-120. https://doi.org/10.1016/j.biosystemseng.2017.08.024

[32] Stanley, H. E., & Meakin, P., 1988. Multifractal phenomena in physics and chemistry. Nature, 335, 405-409. https://doi.org/10.1038/335405a0

[33] Walkley, A., & Black, I. A., 1934. An examination of the Degtjareff method for determining soil organic matter, and a proposed modification of the chromic acid titration method. Soil Science, 37, 29-38.

[34] Wang, B., An, S., Liang, C., Liu, Y., & Kuzyakov, Y., 2021. Microbial necromass as the source of soil organic carbon in global ecosystems. Soil Biology and Biochemistry, 162, 108422. https://doi.org/10.1016/j.soilbio.2021.108422

[35] Yang, L., Lyu, M., Li, X., Xiong, X., Lin, W., Yang, Y., & Xie, J., 2020. Decline in the contribution of microbial residues to soil organic carbon along a subtropical elevation gradient. Science of the Total Environment, 749, 141583. https://doi.org/10.1016/j.scitotenv.2020.141583

[36] Zhang, X., Jia, J., Chen, L., Chu, H., He, J. S., Zhang, Y., & Feng, X., 2021. Aridity and NPP constrain contribution of microbial necromass to soil organic carbon in the Qinghai-Tibet alpine grasslands. Soil Biology and Biochemistry, 156, 108213. https://doi.org/10.1016/j.soilbio.2021.108213

[37] Zhang, Y., Ma, K., Anand, M., & Fu, B., 2006. Do generalized scaling laws exist for species abundance distribution in mountains? Oikos, 115, 81-88.

https://doi.org/10.1111/j.2006.0030-1299.15021.x

[38] Zhang, Z., Liu, L., Huang, M., Chen, F., Niu, J., & Liu, M., 2022. Feasibility of soil erosion measurement using time domain reflectometry. Catena, 218, 106571. https://doi.org/10.1016/j.catena.2022.106571

[39] Zhou, R., Liu, Y., Dungait, J. A., Kumar, A., Wang, J., Tiemann, L. K., ... & Tian, J., 2023. Microbial necromass in cropland soils: A global meta-analysis of management effects. Global Change Biology, 29, 1998-2014. https://doi.org/10.1111/gcb.16613

[40] Zhu, X., Liang, C., Masters, M. D., Kantola, I. B., & DeLucia, E. H., 2018. The impacts of four potential bioenergy crops on soil carbon dynamics as shown by biomarker analyses and DRIFT spectroscopy. GCB Bioenergy, 10, 489-500. https://doi.org/10.1111/gcbb.12520

Figure captions

Figure 1. The location of the 60-ha study site at Jianfengling, the division of 500 quadrats, and the layout of twelve soil cores within each quadrat.

Figure 2. Scatter plot and liner fit of microbial necromass carbon (MNC), soil organic carbon (SOC, a), and plant biomass (PB, b) with correlation coefficient (*r*) and the probability of statistical significance (*p*) given within each figure. Solid lines indicate the regression line from a linear model, grey area represents the 95% confidence interval.

Figure 3. Generalized dimension spectra (a) and singularity spectra (b) of microbial necromass carbon (MNC), soil organic carbon (SOC), and plant biomass (PB).

Figure 4. The joint multifractal spectrum of the spatial variation of microbial necromass carbon (MNC), soil organic carbon (SOC), and plant biomass (PB) (a). The colored scatters corresponding to the joint multifractal spectrum separated individually about SOC (b) and PB (c) at $q = -15$, 0, and 15.

Figure 5. Joint multifractal spectra between microbial necromass carbon (MNC) and soil organic carbon (SOC) for $q_{[PB]} = -15$, 0, and 15. Joint multifractal spectra between MNC and plant biomass (PB) for $q_{[SOC]} = -15$, 0, and 15. The depth of grey represents the normalized values of $f(\alpha_{[MNC]}, \alpha_{[SOC]}, \alpha_{[PB]})$, where black for 1 and white for 0.

Figure 6. Single multifractal spectra of MNC obtained for different $q_{[SOC]}$ and $q_{[PB]}$ scenarios. MNC, microbial necromass carbon; SOC, soil organic carbon; PB, plant biomass.

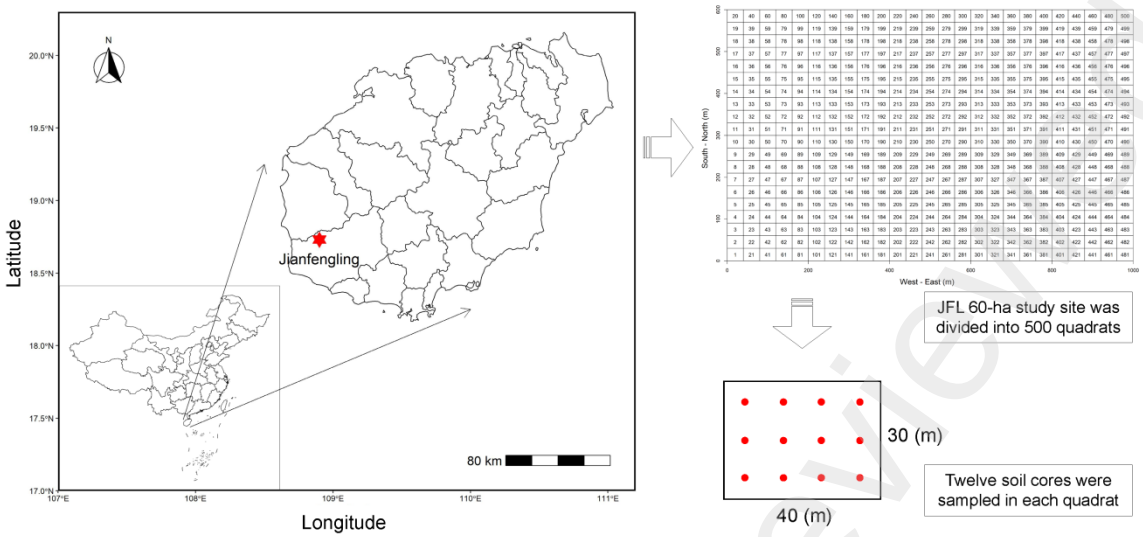

Figure 1

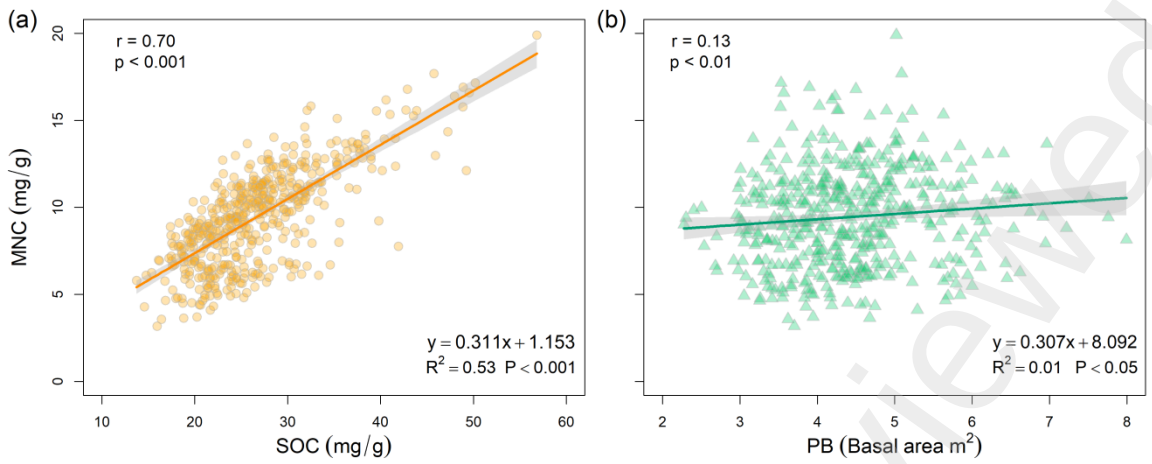

Figure 2

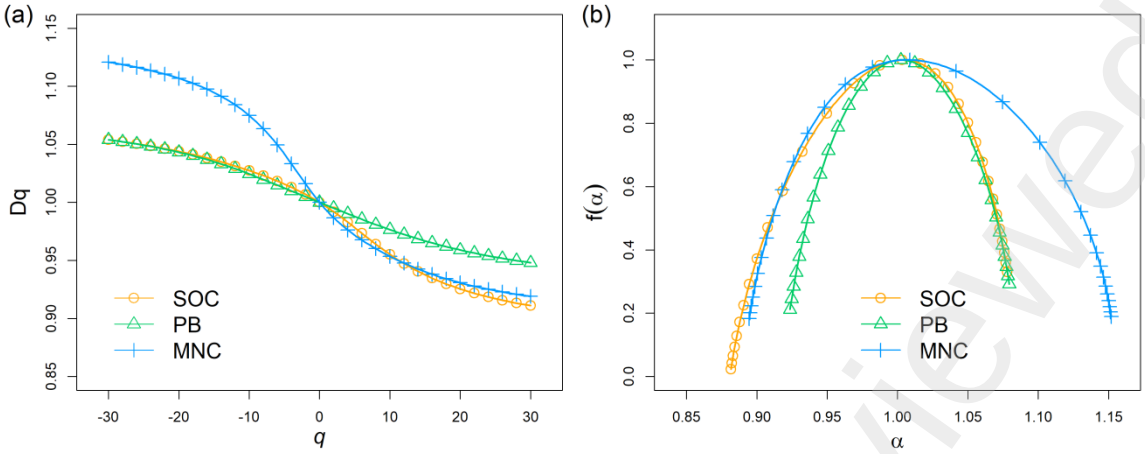

Figure 3

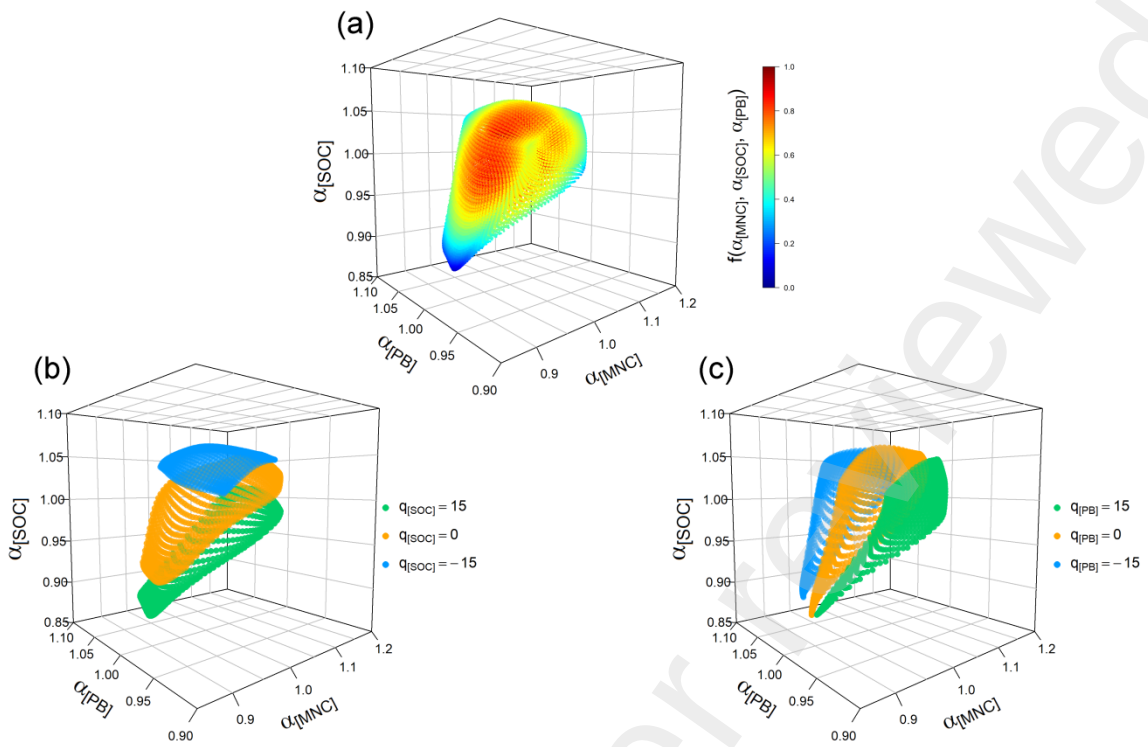

Figure 4

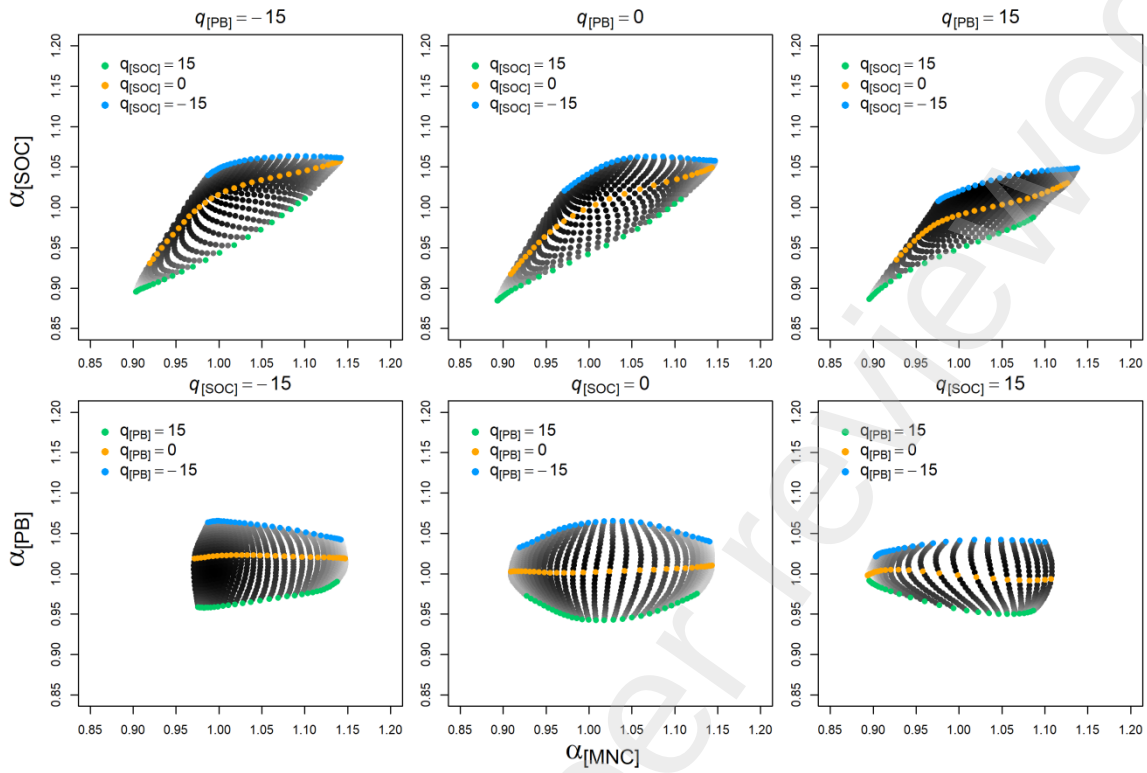

Figure 5

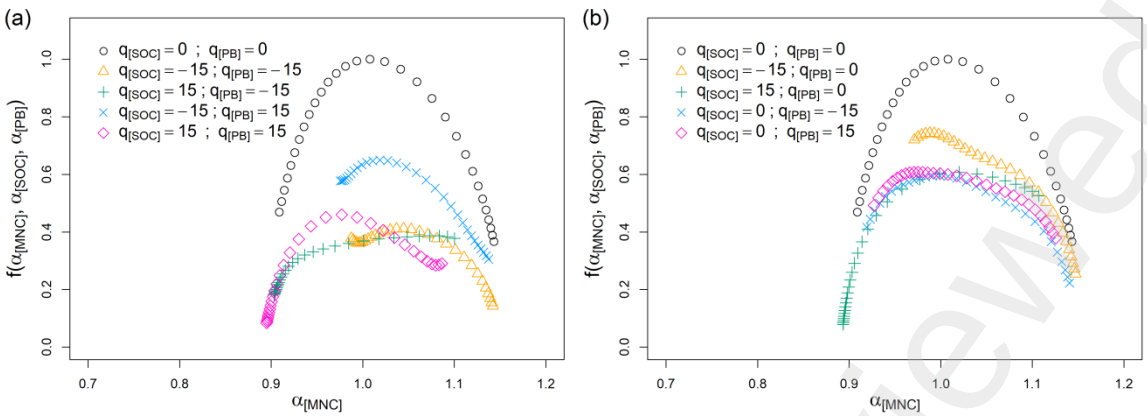

Figure 6

Table 1. Multifractal parameters obtained from the generalized dimension and singularity spectra of microbial necromass carbon (MNC), soil organic carbon (SOC), and plant biomass (PB), (D_{-30}, D_0, D_1, D_2, D_{30}, and ΔD; α_{min}, α_0, α_{max}, $\Delta\alpha$, L and R).

	Generalized dimension spectra (D_q - q)					
	D_{-30}	**D_0**	**D_1**	**D_2**	**D_{30}**	**$D_{-30}-D_{30}$**
MNC	1.121	1.00	0.993	0.987	0.919	0.202
SOC	1.054	1.00	0.996	0.992	0.911	0.143
PB	1.054	1.00	0.998	0.995	0.948	0.106
	Singularity spectra ($f(\alpha)$ - α)					
	α_{min}	**α_0**	**α_{max}**	**$\alpha_{max}-\alpha_{min}$**	**L**	**R**
MNC	0.895	1.009	1.152	0.257	0.114	0.143
SOC	0.882	1.003	1.078	0.196	0.121	0.075
PB	0.924	1.002	1.079	0.155	0.078	0.077